Soft Matter

PAPER

View Article Online
View Journal | View Issue

Cite this: *Soft Matter*, 2025, **21**, 8935

Assessing the dynamics of symmetric and asymmetric hyaluronic acid–chitosan complex coacervates

Roshan Akdar Mohamed Yunus, [a] Roos Poelman,[a] Abinaya Arunachalam, [b] Marleen Kamperman [b] and Daniele Parisi *[a]

Received 8th September 2025,
Accepted 3rd November 2025

DOI: 10.1039/d5sm00910c

rsc.li/soft-matter-journal

The mechanics of complex coacervates are governed not only by electrostatic interactions but also by polymer molecular weight (M_w) and chain stiffness, yet their combined role remains insufficiently resolved for biopolyelectrolytes. We investigate hyaluronic acid (HA)–chitosan (CHI) coacervates across nine symmetric and asymmetric M_w pairings, using rheology, van Gurp–Palmen analysis, and probe-tack adhesion to map salt responsiveness. At 0 M NaCl, when charges are not screened, entangled systems display solid-like behavior, while an unentangled pair behaves as a viscoelastic liquid. All systems show two regimes of plateau modulus (G_N^0): a gradual decrease at low salt content, followed by an abrupt drop beyond a critical salt concentration. Symmetric systems consistently display pronounced modulus decay, whereas asymmetric systems show contrasting responses: long, flexible CHI amplifies salt-induced weakening, while stiff, hydrated HA confers greater resistance and slows modulus reduction. Adhesion measurements reflect the same molecular determinants, showing that chain flexibility enhances interfacial energy dissipation at low salt, whereas chain stiffness promotes adhesion retention at elevated ionic strength. These findings highlight M_w and stiffness, alongside charge density, as central design parameters for coacervates with programmable resilience and adhesion in underwater and biomedical settings.

Introduction

Complex coacervation, or polyelectrolyte complexation (PEC), arises from the electrostatic association of oppositely charged polyelectrolytes, driven in part by counterion release and entropic gains. The resulting polymer-rich coacervate phase typically exhibits high water content and viscoelastic liquid behavior, with properties that depend on pH, ionic strength, and temperature.[1–12] Complex coacervation has gained significant attention as a versatile technique for making functional materials for widespread applications ranging from underwater adhesives, membranes, drug delivery, 3D printing, fiber processing, tissue engineering, food, and cosmetic industries.[4,9,10,12–27]

A key advantage of coacervates is the tunability of their rheology. Indeed, their mechanical properties can be controlled *via* polymer chemistry, molecular weight (M_w), mixing ratio, charge density, pH, and salt type.[3,7,8] Rheology has proved central to understanding coacervate dynamics, phase behavior, and printability.[2,4,5,11,28] A recent review by R. G. Larson *et al.*[3] provides a comprehensive overview of the rheological findings for various polyelectrolyte complexes, emphasizing the role of time–salt superposition (tSS), an analogue of time–temperature (tTS), for comparing frequency sweeps at different salt concentrations.[3,7]

The idea of tSS was first introduced by Cohen Stuart and co-workers,[1] who showed that frequency sweeps at varying salt concentrations could be shifted along frequency and modulus axes to form master curves. This implies that the relaxation dynamics of the polymer chains scale solely with salt concentration.[1,2] Subsequent studies confirmed tSS across diverse chemistries.[3,5–7,28–38] Related approaches generated master curves by varying pH, temperature, ionic strength, alcohol, water, and hydrophobicity.[3,5–7,29,32,33,35,36,39–45] However, the superposition principles carry major limitations with them. Superposition is typically valid only within a limited frequency or time range, as changing the salt, temperature (or other parameters) can alter the dominant relaxation mechanisms and even the physical state of the coacervate. Shift factors often deviate from universal predictions, reflecting the interplay of charge density, M_w, hydrophobicity, and secondary

[a] *Department of Chemical Engineering, Engineering and Technology Institute Groningen, University of Groningen, Nijenborgh 3, 9747 AG Groningen, The Netherlands. E-mail: d.parisi@rug.nl*
[b] *Zernike Institute for Advanced Materials, University of Groningen, Nijenborgh 3, Groningen 9747 AG, The Netherlands*

interactions.[3] Phase heterogeneity and salt partitioning can further prevent universal scaling, with deviations most pronounced at low frequencies where additional relaxation modes emerge.[3] Hence, the superposition principles cannot be said to be universally applicable. In this context, the van Gurp–Palmen (vGP) plot represents a sensitive tool to assess superposability, correlating phase angle with complex modulus to reveal structural inhomogeneity.[46] Importantly, the vGP plot helps verify the applicability of superposition principles by testing whether data at different conditions collapse onto a single master curve. Deviations from this overlap can signal changes in the relaxation spectrum or fundamental differences in microstructure.[47,48]

While synthetic PECs often conform to tSS,[3,5–7,28–38] biopolymers exhibit additional relaxation pathways due to chain rigidity, polydispersity, supramolecular interactions, hydrogen bonding, hydration, and hydrophobic effects.[49–51] These could potentially alter the relaxation dynamics, making them insensitive to uniform salt scaling.

Rubinstein *et al.*[52] showed that relaxation in polyelectrolyte coacervates reflects a balance between electrostatic crosslinks and entanglement, with chain rigidity and molecular weight controlling salt sensitivity. At low salt, elasticity stems from electrostatic associations, while added salt shortens correlation lengths and disrupts associative bridges, leading to gradual softening in rigid, highly entangled systems. In their follow-up work, Rubinstein and co-workers[53] demonstrated that flexible chains yield sharper salt-induced softening, developing a scaling theory where stiff, high-M_w polyelectrolytes form salt-resistant networks and flexible chains produce rapid relaxation.

The review by R. G. Larson *et al.*[3] also highlighted that chain-length asymmetry adds further complexity. Spruijt *et al.*[2] observed that polycation length more strongly affects dynamics than polyanion length in PDMAEMA/PAA coacervates, while Liu *et al.*[34] noted an apparent dominance of the polycation response in PTMAEMA/PSPMA systems but attributed this trend primarily to minor differences in actual molecular weight. Conversely, Hamad *et al.*[38] found polyanion length more influential in PDADMA/IBMA-Na complexes. Consequently, R. G. Larson *et al.*[3] proposed in their Review that this behavior can be attributed to differences in their monomer hopping distances after ion pair dissociation. If polycation monomers, due to chain rigidity or other factors, move shorter distances than polyanion monomers before reforming transient ion pairs (rebinding) with oppositely charged sites, polycation chains will relax more slowly. As a result, the polyelectrolyte with the longest chain length has a greater influence on relaxation time. Since monomer diffusivity depends on the square of the hopping distance, even a modest difference can lead to a significant asymmetry in relaxation behavior.[3] These seminal works highlight the importance of chain stiffness, molecular weight asymmetry, and their contribution to the rheological properties of complex coacervates. Despite these insights, the interplay between polymer flexibility and molecular weight asymmetry in biopolymer coacervate systems remains insufficiently explored.

Hyaluronic acid (HA) and chitosan (CHI) represent an important model system due to their natural origin, biocompatibility, and tunability.[28] HA is a highly hydrated polyanion, and CHI is a polycation obtained from naturally occurring chitin; the structures of both these biopolymers are illustrated in Fig. 1a and b, respectively.[28,50,51] HA/CHI coacervates are sought for their applications in making fibers, hydrogels, scaffolds, and targeted therapeutics.[25,54–58] Additionally, the biocompatible and non-toxic nature of these biopolymers also opens doors to the application of these materials as underwater or medical adhesives.[59] Kayitmazer *et al.*[59] showed that varying HA or CHI M_w alters rheology, but a systematic understanding of how symmetry *versus* asymmetry controls dynamics under salt variation is lacking.

In this work, we address these gaps by systematically studying a library of nine HA–CHI coacervate systems that vary in molecular weight pairing: three symmetric systems (lowHA_lowCHI, medHA_medCHI, highHA_highCHI; for the color coding used in labelling the systems in this work, see Fig. 1c) and six asymmetric systems with varied degrees of mismatch between HA and CHI molecular weights (see Table 1). The overview of the preparation technique and testing is illustrated in Fig. 1d (for further details, see Experimental section). A combination of oscillatory shear rheology and probe-tack adhesion is used to test the effect of polymer molecular weight and asymmetry on the coacervate phase behavior, dynamics, and adhesion under changing ionic conditions. Throughout, "symmetric" denotes approximate M_w balance based on average values, acknowledging the inherent polydispersity of HA and CHI.

Experimental

Materials and coacervate preparation

Chitosan (CHI, degree of deacetylation 89%) with average M_w of 30 kDa (low), 250 kDa (medium), and 890 kDa (high) was purchased from Glentham Life Sciences (UK). Sodium hyaluronate (HA) with M_w of 30–50 kDa (low), 200–400 kDa (medium), and 750–1000 kDa (high) was also obtained from Glentham Life Sciences (UK). According to the vendor datasheets, these are reported as "average molecular weights," without specification of whether they represent number-average (M_n), weight-average (M_w), or viscosity-average (M_v) values, and no experimental method (*e.g.*, size exclusion chromatography or viscometry) is provided. These values are therefore used here as indicative of relative molecular size rather than absolute M_w. All polymers were used as received. Sodium chloride (NaCl), hydrochloric acid (HCl), and sodium hydroxide (NaOH) were from Sigma-Aldrich (Germany). Deionized (DI) water was prepared by reverse osmosis (conductivity <10 μS cm^{-1}). Stock solutions of HA and CHI (10 mg mL^{-1}, pH 4) were prepared separately. CHI was first dispersed in DI water, the suspension acidified to pH 2 with 5 M HCl and stirred until clear (30 min to 8 h depending on M_w). The pH was then raised to 4 with 0.5 M NaOH, and the solution was stirred for another 30 min. HA was directly dissolved in DI water (1–8 h stirring, depending on M_w), adjusted to pH 4 with 1 M HCl, and homogenized for 30 min. Coacervates at ionic strengths of 0.0–0.8 M NaCl were prepared by mixing HA stock with DI water and 5 M NaCl to the desired

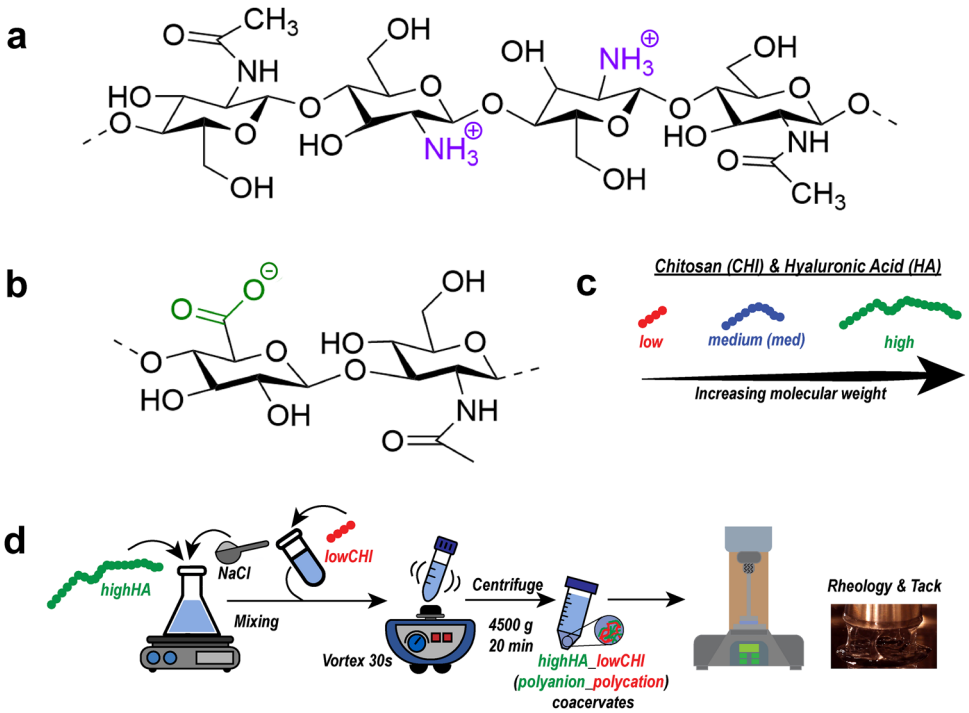

Fig. 1 Schematic representation. Chemical structure of the polycation, chitosan CHI (a) and the polyanion hyaluronic acid HA (b) at pH 4. The purple-colored moiety in (a) represents the positively charged group in CHI, making it the polycation, whereas the green-colored moiety in (b) represents the negatively charged unit in HA, making it the polyanion. (c) The colors red, dark blue, and green indicate low, medium (med), and high M_w (the M_w numbers can be found in the Experimental section), respectively. (d) Illustration of the preparation of complex coacervates used in this work.

final salt concentration, vortexing 30 s, and adding the corresponding CHI stock. The relative volumes of HA and CHI were calculated to maintain a 1 : 1 charge ratio between carboxylate (COO^-) and ammonium (NH_3^+) groups, corresponding to feed concentrations of $\sim$4.8 mg mL^{-1} HA and $\sim$2.2 mg mL^{-1} CHI in the 10 mL mixtures. Mixtures were vortexed for 2 min, centrifuged at 4500*g* for 20 min at 20 °C, and the dense HA–CHI coacervate phase was separated for further tests. All reported salt concentrations refer to added NaCl. The intrinsic counterions associated with the charged biopolymers were not removed prior to mixing, and thus a baseline ionic strength from these counterions is inherently present in all samples. While the charge balance and total feed polymer concentration are well-defined, the actual polymer content within the separated coacervate phase is expected to be higher than in the feed and to vary with ionic strength, as a small fraction of polymer remains in the supernatant following phase separation.

Table 1 Critical salt concentration limits (determined from UV-vis spectroscopy) for the various complex coacervates investigated in this work

System	Critical salt limit (M)
lowHA_lowCHI	0.6
lowHA_medCHI	0.8
lowHA_highCHI	0.8
medHA_lowCHI	0.6
medHA_medCHI	0.9
medHA_highCHI	0.9
highHA_lowCHI	0.6
highHA_medCHI	0.9
highHA_highCHI	0.9

UV-Vis spectroscopy

Optical transmittance was measured at 600 nm using a Hitachi U-1800 spectrophotometer and a 1 cm-pathlength quartz cuvette. Measurements were performed immediately after mixing HA, NaCl, and CHI solutions.

Shear rheology

Measurements were carried out on an MCR302e strain-controlled rheometer (Anton Paar, Germany) with parallel-plate geometry (10 or 25 mm). All tests were conducted at 20 °C using a Peltier plate with supernatant added around the sample to minimize evaporation. Samples were pre-conditioned by dynamic time sweeps (DtS) at 1 rad s^{-1} and large strain amplitude (from prior dynamic strain sweeps) to erase the mechanical history of the sample (typically 60–100 s). DtS in the linear viscoelastic regime was then performed to follow the aging of the system, until steady state moduli were attained (typically 200 s). Linear viscoelastic behavior was then probed *via* frequency sweeps (small amplitude oscillatory shear) performed from 100 to 0.01 rad s^{-1}.

Probe tack testing

Adhesion was measured with the same rheometer equipped with a 10 mm sandblasted stainless-steel probe. The lower plate was held at 20 °C. The probe was lowered to a 150 μm gap and held for 60 s before retraction at 100 μm s^{-1}. Normal force was

recorded *versus* displacement and converted into nominal stress–strain curves. Work of adhesion (W_{adh}) was calculated as the area under the curve multiplied by the initial sample thickness.[5] Values are reported as means of three independent replicates.

Results and discussion

Complex coacervation

Hyaluronic acid (HA) and chitosan (CHI) of varying M_w (see Experimental) were mixed at different salt concentrations at pH 4. This pH was chosen because both HA and CHI are fully ionized: all carboxylate groups on HA and amino groups on CHI remain charged.[28] The charge ratio between negatively and positively charged units was fixed at 1.[5,28,58,60] To probe how M_w asymmetry affects salt stability, turbidity was monitored by UV-vis spectroscopy. Fig. 2a–i shows transmittance as a function of NaCl concentration for nine HA–CHI combinations with different M_w pairings. The critical salt limit (CS) was defined as the concentration at which transmittance exceeded ~80%, signifying dissolution of the coacervate phase and reversion to a single homogeneous solution.[61] The CS limits of all systems are listed in Table 1.

Increasing the molecular weight (M_w) of one or both polyelectrolytes enhances salt resistance, with medium- and high-M_w CHI consistently yielding the most stable coacervates, while systems with low-M_w CHI or HA show lower CS values. This trend reflects the thermodynamics of coacervate formation. Below the CS, electrostatic attractions between oppositely charged chains dominate and drive liquid–liquid phase separation.[19] As salt concentration rises, these interactions are progressively screened, reducing favorable ion pairing and increasing the free energy until phase separation becomes unfavorable.[15,62,63] Recent calorimetric analysis of HA–CHI coacervates[64] further demonstrated that coacervation is predominantly driven by counterion-release entropy, while ion-pairing enthalpy becomes increasingly favorable with molecular weight due to cooperative electrostatic interactions. This trend supports our interpretation that the enhanced salt resistance of high-M_w systems arises from cooperative and multivalent electrostatic binding. The enhanced resistance at higher M_w originates from cooperative binding and entropy. Longer chains present more binding sites, so once one site binds, subsequent associations are favored, strengthening the network.[61,65] In addition, the Flory–Huggins theory predicts that longer polymers reduce the entropy of mixing, diminishing miscibility and requiring higher salt concentrations to disrupt the complex.[61] Interestingly, increasing the molecular weight of CHI is much more effective at enhancing salt resistance than increasing that of HA. This discrepancy can be understood in terms of polymer chain flexibility. HA is relatively stiff, with an electrostatic persistence length (p) of ~4–10 nm, while CHI is more flexible, with an electrostatic persistence length of ~1–4 nm under salt conditions comparable to those used in this study.[66,67] In addition to this difference in flexibility, CHI has a higher linear charge density, with an average charge spacing of ~0.57 nm compared to ~1.02 nm for HA.[68,69] This closer charge spacing enhances electrostatic binding and contributes to the greater salt resistance observed in CHI-rich systems. While chain rigidity is likely the dominant factor, one cannot fully exclude secondary contributions from CHI's hydroxyl-mediated hydrogen bonding or weak hydrophobic interactions. However, at pH 4, electrostatic interactions dominate, making hydrogen bonding comparatively minor, and the full charge on CHI largely masks hydrophobic patches, so these effects are expected to play only a limited role under our conditions. The increased flexibility of CHI allows longer chains to adopt conformations that facilitate multivalent interactions and entanglements, thereby forming more robust and resilient networks.[70–72] In contrast, the stiffness of HA limits its ability to exploit longer chain lengths for cooperative binding or network formation.[70–72] As such, systems with high molecular weight CHI and low-to-medium M_w HA show disproportionately high CSs compared to systems where only HA's molecular weight is increased. This asymmetry agrees with Kayitmazer *et al.*,[59] who showed that long CHI enhances entanglement and prolongs relaxation in HA–CHI coacervates, stabilizing electrostatic networks under salt stress. Fig. 2j illustrates this effect for lowHA_medCHI, where turbidity decreases gradually with increasing salt and only faint cloudiness remains at 0.7 M NaCl, matching the UV-vis transition.

Overall, salt resistance in HA–CHI coacervates is dictated by both M_w and chain flexibility. Flexible, high-M_w CHI plays a disproportionate role in stabilizing networks, while stiff HA contributes less with increasing M_w. These results emphasize the need to consider polymer conformation and dynamics, not just charge or size, when designing coacervates with tailored stability.

Linear viscoelasticity

Fig. 3 depicts the small-amplitude oscillatory shear (SAOS) measurements performed on lowHA_lowCHI, medHA_medCHI, and highHA_highCHI coacervates at 0, 0.2, and 0.5 M NaCl. Storage modulus (G'), loss modulus (G''), and complex viscosity (η^*) across angular frequencies (ω) provide insight into the relaxation behavior of PECs.

At 0 M NaCl (Fig. 3a), lowHA_lowCHI exhibits liquid-like behavior with a crossover at high ω, below which G'' exceeds G', consistent with the structural relaxation of an entangled system.[2,3,28,35] By contrast, medHA_medCHI and highHA_highCHI show $G' > G''$ across the entire frequency window, with no terminal regime within 100 s (0.01 rad s^{-1}), characteristic of dynamically arrested systems.[73–78] This reflects increased chain length, entanglement density,[38,41,59,70] and strong electrostatic interactions.[2,3,41]

Panel 3b shows the corresponding complex viscosity curves. LowHA_lowCHI has substantially lower η^* values compared to the medium and high M_w systems, which were all prepared at the same total polymer concentration and charge stoichiometric ratio, and displays a Newtonian plateau at low ω, indicating faster relaxation dynamics. Both medHA_medCHI and highHA_highCHI shear thin at high ω, hinting at a plateau

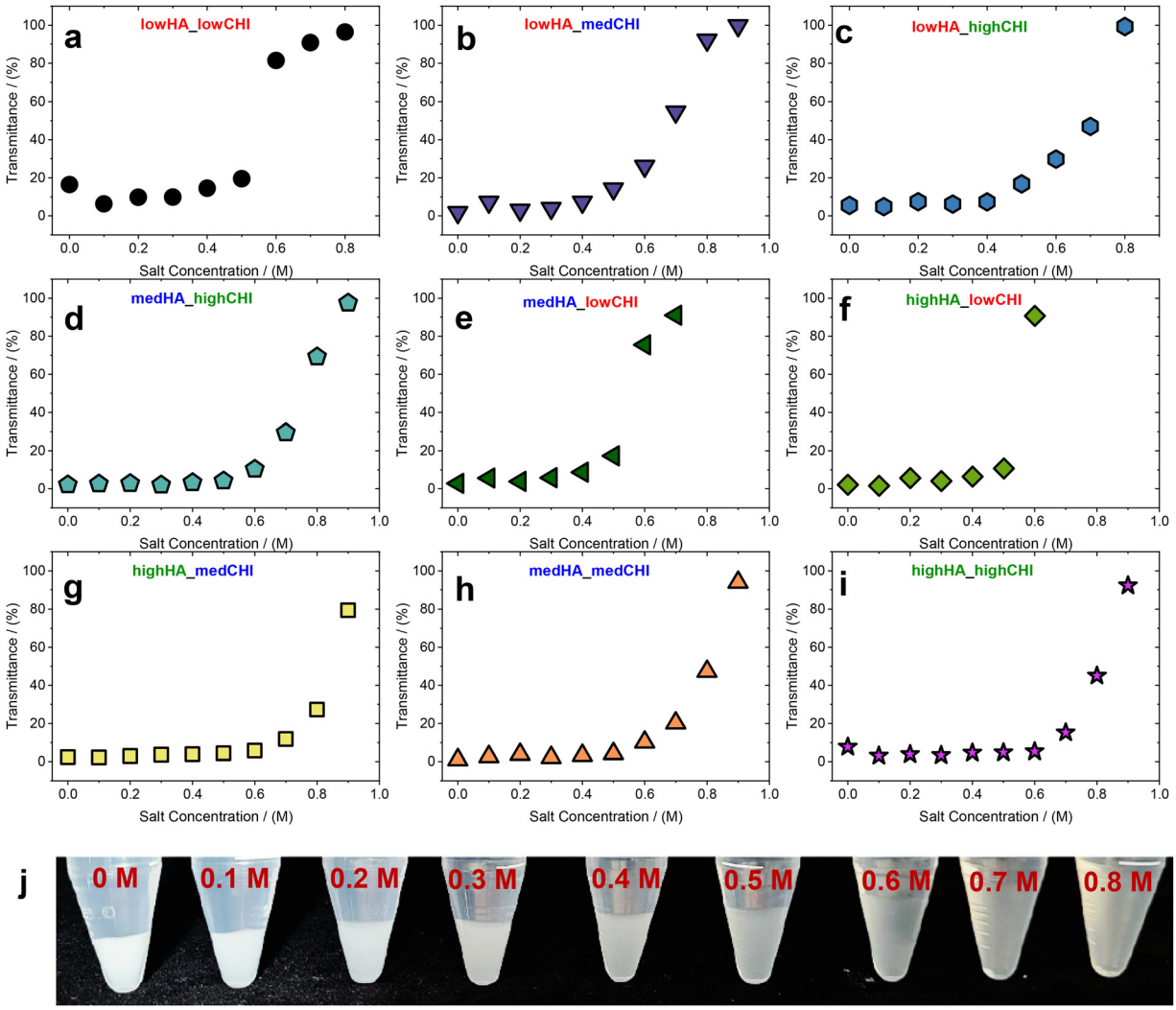

Fig. 2 UV-Vis spectroscopy. (a)–(i) Evolution of the transmittance determined by UV-vis spectroscopy upon the addition of CHI solutions (of varying M_w) to HA solutions (of varying M_w) as a function of NaCl concentration. The pairs of polyanion–polycation are labeled in their respective plots. (j) Images of complex coacervates obtained from HA–CHI (lowHA_medCHI) samples of varying salt concentrations in the range 0.0–0.8 M NaCl, after centrifugation.

at low ω, indicating slower structural relaxation. At low ω, highHA_highCHI exhibits higher η^* than medHA_medCHI, consistent with higher M_w chains.

At 0.2 M NaCl (Fig. 3c and d), qualitative trends persist, but moduli and viscosities decrease due to partial charge screening. LowHA_lowCHI becomes fully liquid-like ($G'' > G'$ across all ω), while medHA_medCHI and highHA_highCHI retain solid-like behavior with a reduced modulus gap. HighHA_highCHI maintains slightly slower dynamics.

At 0.5 M NaCl (Fig. 3e and f), electrostatic interactions are further weakened, and this is reflected in significantly reduced moduli and viscosities. The lowHA_lowCHI system becomes fully liquid-like, with $G'' > G'$ throughout. Both medHA_medCHI and highHA_highCHI now exhibit a clear crossover in G' and G'' at lower frequencies, marking the onset of the terminal flow regime. The crossover frequency is lower for highHA_highCHI than for medHA_medCHI, indicating that the former still retains more elasticity and slower relaxation dynamics. In panel 3f, η^* curves confirm these findings: lowHA_lowCHI again displays a clear Newtonian plateau at low ω, while the medium and high M_w systems continue to show shear-thinning behavior that trends toward Newtonian behavior at longer timescales. The slower dynamics of highHA_highCHI compared to medHA_medCHI arise from higher entanglement density and cooperative electrostatic binding.[3,38,70] Longer chains form denser networks that delay terminal relaxation, while short-time responses remain comparable. Because these systems are molecularly symmetric, differences in viscoelasticity reflect the direct effect of M_w. The observed increase in elasticity, viscosity, and salt resistance with rising M_w thus originates from entanglement and cooperative binding in matched-M_w coacervates.

Fig. 4 shows the linear viscoelastic response of the low-HA_lowCHI system, formed from low-M_w HA and CHI. This weakly entangled coacervate is a viscoelastic liquid.[70] Frequency sweeps of storage (G') and loss (G'') moduli, complex

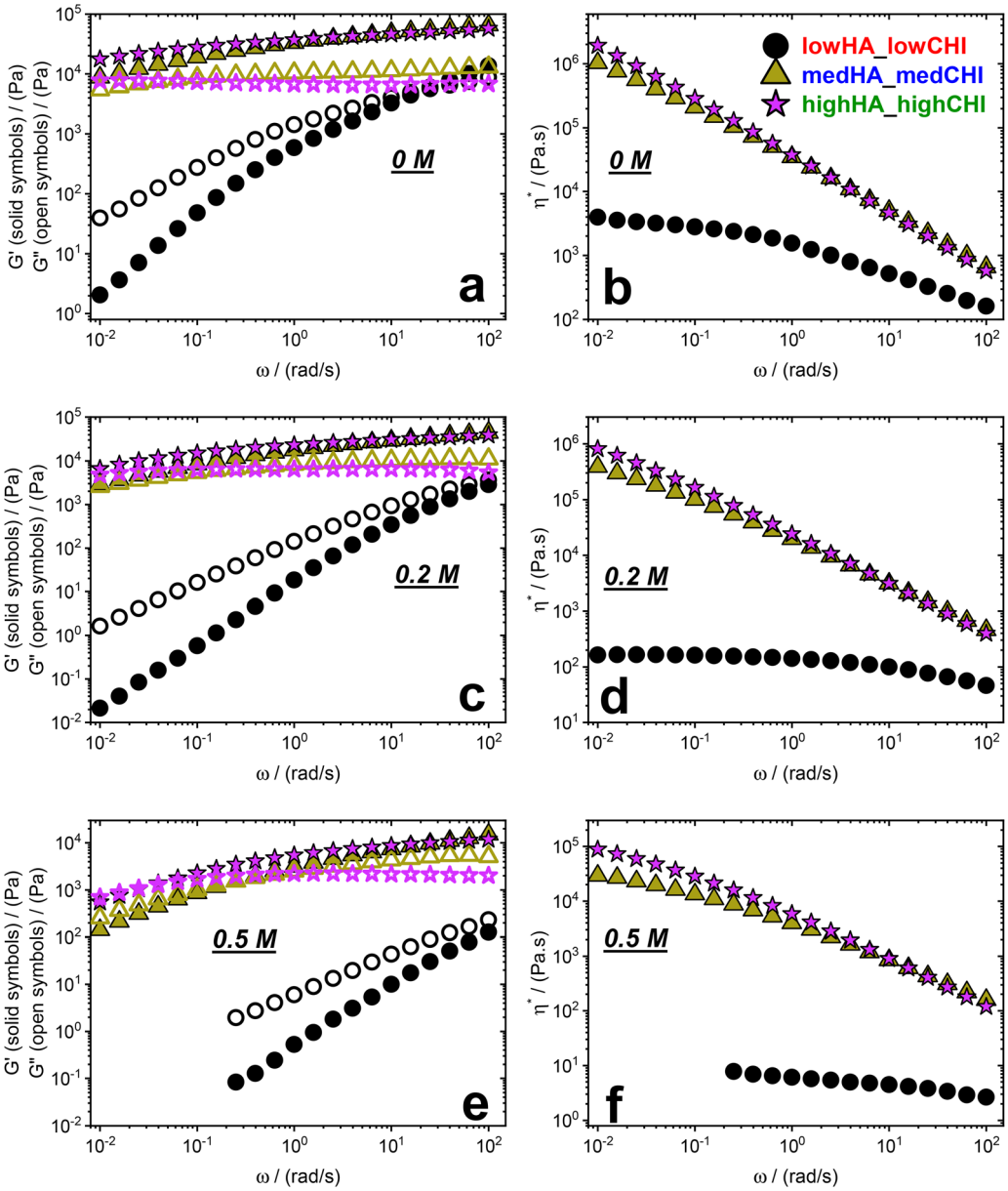

Fig. 3 Linear viscoelasticity of symmetrical pairs. Storage modulus G' (closed symbols), loss modulus G'' (open symbols), and complex viscosity η^*, as a function of oscillation frequency ω for the symmetric M_w samples across three different salt concentrations (a) and (b) 0 M, (c) and (d) 0.2 M, and (e) and (f) 0.5 M. The labels are color-coded for ease of perusal. The colors red, dark blue, and green indicate low, medium, and high M_w, respectively.

viscosity (η^*), loss factor ($\tan\delta$), and van Gurp–Palmen (vGP) plots are presented for salt concentrations of 0–0.5 M NaCl. At 0 M (Fig. 4a), the system exhibits liquid-like behavior with a G'–G'' crossover at high ω, followed by $G'' > G'$ over the remaining range. Adding 0.1 M salt shifts the crossover to higher ω, reflecting faster dynamics from weakened electrostatic association. At 0.3 M and above, no moduli crossover is observed within the experimental window, highlighting strong plasticization: electrostatics are increasingly screened, and relaxation dynamics accelerate. Viscosity profiles (Fig. 4b) support this picture. At 0 M, η^* decreases with ω and shows a faint Newtonian plateau at low ω. With added salt, η^* drops markedly and approaches Newtonian behavior at higher ω, consistent with enhanced chain mobility. Tan δ curves (Fig. 4c) confirm the elastic-to-viscous shift. At 0 and 0.1 M, $\tan\delta < 1$ at high ω indicates elastic dominance, whereas at higher salt concentrations $\tan\delta > 1$ across the entire window, signifying viscous-dominated relaxation. Finally, vGP plots (Fig. 4d) show good overlap of curves up to 0.4 M, near the critical salt limit, indicating that the relaxation spectrum scales across these conditions.[1] This data collapse demonstrates the partial applicability of time–salt superposition (tSS) in this system, consistent with earlier reports.[28,35]

After validating data collapse in the vGP representation, SAOS datasets were shifted horizontally using the 0 M system as a reference. Fig. 5 illustrates the tSS results. In Fig. 5a, the

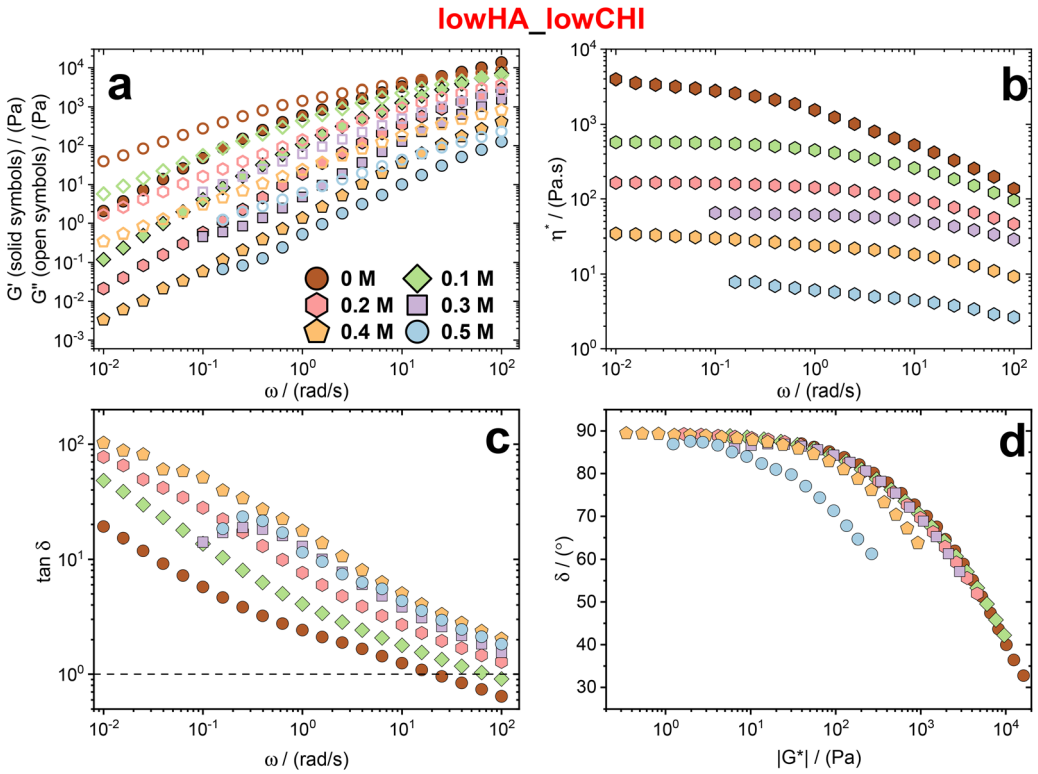

Fig. 4 Linear viscoelasticity of lowHA_lowCHI. (a) Storage modulus G' (closed symbols), loss modulus G'' (open symbols), and (b) complex viscosity η^*, as a function of oscillation frequency ω for the complex coacervates formed from low M_w HA and low M_w CHI across varying salt concentrations (see legend). Additionally, the loss factor $\tan\delta$, derived from SAOS, expressed as a function of oscillation frequency ω and the van Gurp–Palmen representations for the coacervates at different salt contents (see legend), are shown in panels (c) and (d), respectively. The black dashed line in (c) represents a $\tan\delta$ value of 1.

frequency dependence of $\tan\delta$ defines the system's states, exhibiting solid- or liquid-like behavior. The master curve in terms of dynamic moduli generated by tSS is reported in Fig. 5(b), spanning six decades in frequency, and serving as the mechanical fingerprint of the system at 0 M NaCl. The material shows the features of a marginally entangled system at high ω ($G' > G''$), followed by a crossover into the terminal regime, consistent with viscoelastic liquid behavior. It is worth noting that our present analysis uses added-salt concentration as a variable and does not explicitly account for counterion contributions. A more complete description incorporating total ionic strength, as proposed by Syed and Srivastava,[29] would be a valuable future extension of this work.

The horizontal shift factor, a_s, which quantifies the acceleration or deceleration of relaxation dynamics with salt, follows the relationship:[1]

$$\ln a_s = B - A\sqrt{c_{salt}} \quad (1)$$

where c_{salt} represents the concentration of the salt, A and B are fitting parameters.

Eqn (1) was first reported by Spruijt *et al.*[1] to describe how salt screens electrostatic interactions. The term $\sqrt{c_{salt}}$ reflects the Debye–Hückel screening, where high salt content accelerates the dynamics and collapses the coacervate networks.[1,3] In this equation, the term A represents the sensitivity of the system to salt; higher A values indicate stronger electrostatics (*i.e.*, higher charge density) and are linked to the activation energy of the system ($A \propto$ energy barrier/k_BT).[3] On the other hand, the parameter B is a constant that incorporates non-electrostatic contributions, *i.e.*, the intrinsic relaxation dynamics of the coacervate system.[3]

The a_s values of the lowHA_lowCHI coacervate system are shown in the inset of Fig. 5a. Similar fitting of horizontal shift factors has been reported in other systems.[1–3,29,38,39,79] The A value obtained for the lowHA_lowCHI coacervate system is 7.8, close to 6.8 reported for PDADMA/PSS coacervates.[39] By contrast, PVBTMA/PSS systems with NaBr yielded A = 12.85,[79] reflecting the chemical specificity of PVBTMA and the larger, more polarizable Br^- ion.[80] Similarly, the A factor for PDMAEMA/PAA with KCl salt is reported to be 12.[2] Thus, A is highly sensitive to salt type and electrostatic strength, with higher values indicating stronger salt-activated dynamics and faster relaxation.

Overall, these results show that in non-entangled coacervates such as lowHA_lowCHI, salt primarily modulates relaxation times without introducing new dissipation modes. The consistent scaling across salt concentrations supports tSS as a robust predictive framework for weakly associated, viscoelastic coacervates.

To contrast unentangled and entangled systems, we examined the highHA_highCHI pair (Fig. 6), where both polyelectrolytes are high-M_w. Unlike the lowHA_lowCHI system (Fig. 4),

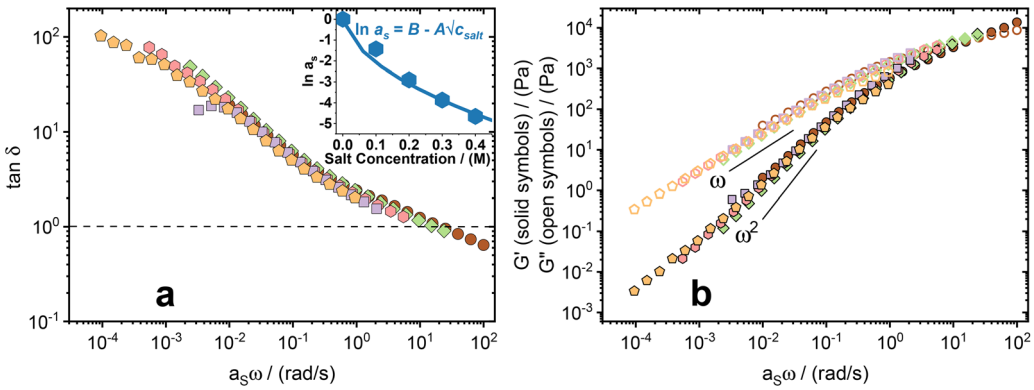

Fig. 5 Time-salt superposition. (a) Loss factor tan δ as a function of the product of oscillation frequency ω and horizontal shift factor a_s. The black dashed line in (a) represents a tan δ value of 1. Solutions with tan $\delta < 1$ mainly show an elastic response, whereas those with tan $\delta > 1$ primarily display viscous behavior. (b) The time–salt superposition (tSS) master curves depicting storage G' (closed symbols) and loss G'' (open symbols) moduli as a function of oscillation frequency ω shifted with horizontal shift factor a_s. The black solid line in (b) represents the terminal slopes of a fully relaxed viscoelastic liquid. The inset in (a) represents ln a_s as a function of the salt NaCl concentration, and the solid line is the fitting line of eqn (1) (also shown in the inset).

this entangled network deviates strongly from ideal time–salt superposition (tSS). At 0 M NaCl (Fig. 6a), $G' > G''$ across the full frequency range, with no crossover, indicating a highly elastic network with slow relaxation, driven by long-chain entanglements and electrostatic interactions.[59] Adding 0.1 M NaCl produces little change at high ω but a modest reduction at low ω. At 0.2 M, G' decreases more noticeably while G'' is largely unchanged, suggesting weakening of the elastic network without terminal relaxation. At 0.3 M, a clear G'–G'' crossover appears, and G' decreases sharply, marking the onset of fluid-like behavior. At higher salt, both moduli continue to decline, and the crossover shifts to higher ω, consistent with

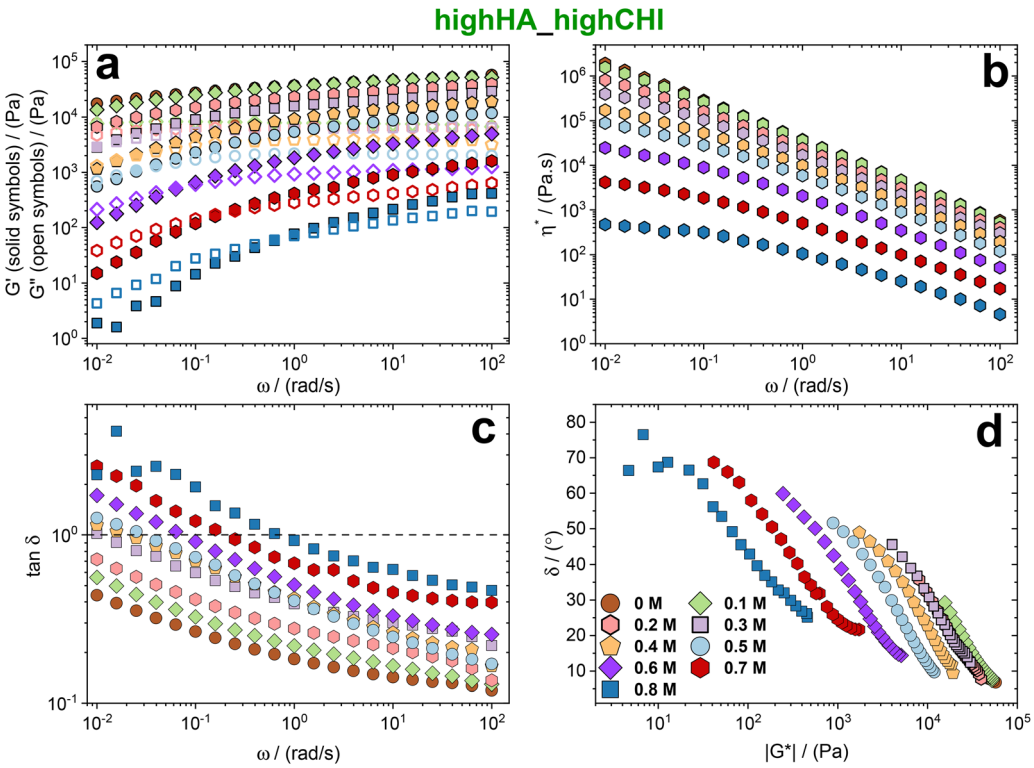

Fig. 6 Linear viscoelasticity of highHA_highCHI. (a) Storage modulus G' (closed symbols), loss modulus G'' (open symbols), and (b) complex viscosity η^*, as a function of oscillation frequency ω for the complex coacervates formed from high M_w HA and high M_w CHI across varying salt concentrations (see legend). Additionally, the loss factor tan δ, derived from SAOS, expressed as a function of oscillation frequency ω and the van Gurp–Palmen representations for the coacervates at different salt contents (see legend) are shown in (c) and (d), respectively. The black dashed line in (c) represents a tan δ value of 1. Solutions with tan $\delta < 1$ mainly show an elastic response, whereas those with tan $\delta > 1$ primarily display viscous behavior.

progressive plasticization and network disruption. Viscosity trends (Fig. 6b) echo this evolution. At 0 M, η^* is nearly frequency-independent, reflecting an elastic network. At 0.1 M, the profile remains similar, but by 0.3 M, η^* decreases strongly, and at higher salt content, a low-frequency Newtonian plateau emerges, confirming liquid-like behavior. Tan δ profiles (Fig. 6c) reinforce this picture: $\tan\delta < 1$ up to 0.3 M indicates elasticity, while values >1 at 0.4 M and above reflect increasing viscous dissipation.

Most critically, vGP plots (Fig. 6d) show no collapse across salt concentrations. Only the 0 and 0.1 M curves overlap; higher salt curves deviate, revealing strong dynamic heterogeneity. Unlike unentangled systems, where relaxation modes scale uniformly with salt, entangled systems introduce salt-insensitive modes such as reptation, constraint release, or hydration-mediated processes, breaking superposability. Similar behavior was observed in other HA–CHI combinations (Fig. S1–S7). Only the nearly entangled lowHA_lowCHI system (Fig. 4 and 5) obeyed tSS. Prior studies have reported apparent tSS in entangled synthetic PECs,[2,33,38] but these systems differ fundamentally from natural biopolymers. Synthetic polymers often have uniform architectures, whereas HA and CHI are polydisperse, heterogeneously charged, and structurally rigid.[50,51,66,67] These features introduce slower relaxation modes and hydration effects that disrupt scaling. One report demonstrated apparent tSS in HA–CHI coacervates.[35] However, their frequency sweeps were limited (100–1 rad s^{-1}) compared to the broader range explored here (down to 0.01 rad s^{-1}), omitting slower relaxation modes. Moreover, van Gurp–Palmen plots were not used, limiting sensitivity to low-frequency deviations. Their overlap at high ω may therefore mask underlying complexity.

It is thus plausible that the biopolymeric origin of HA and CHI, with their higher stiffness (in the case of HA), stronger hydration shells, and biologically evolved structural complexity, leads to decoupling between electrostatic screening and network relaxation processes.[50,51,66,67] This decoupling may explain why even entangled systems do not obey tSS in our case, in contrast to synthetic counterparts. While synthetic polymers can certainly be engineered to incorporate features such as backbone rigidity, hydrogen-bonding motifs, or hierarchical structures, what distinguishes natural biopolymers is the intrinsic co-occurrence of these attributes within the same macromolecule. These observations underscore the need for tailored scaling frameworks for biopolymer-based coacervates and highlight the limitations of directly applying principles derived from synthetic systems to natural materials.

The terminal relaxation time, τ_D, quantifies the stress-relaxation timescale of coacervates and reflects polymer mobility and interaction strength.[3] Because ionic screening strongly influences coacervate dynamics, tracking τ_D *versus* salt provides mechanistic insight into how electrostatics and chain architecture govern relaxation.

The τ_D values in Fig. 7 were calculated as the inverse crossover frequency from the SAOS measurements. In Fig. 7a, we compare the salt-dependent terminal relaxation behavior of two symmetric coacervate systems: medHA_medCHI and highHA_highCHI. Both systems exhibit a clear decrease in τ_D with increasing salt concentration, reflecting the expected weakening of electrostatic interactions and an increase in polymer chain mobility.[2,11,28,35,41] However, the extent of this dependence varies significantly with molecular weight. Specifically, highHA_highCHI displays a slightly weaker decrease in τ_D (scaling exponent ~ -9) compared to medHA_medCHI (scaling exponent ~ -10), indicating a reduced sensitivity to ionic screening. This behavior can be attributed to the greater entanglement density and intrinsic stiffness of the higher molecular weight of HA, which give rise to more constrained dynamics. This is consistent with the theoretical framework in Rubinstein *et al.*,[52] which emphasizes that at high molecular weights, relaxation is increasingly governed by entanglement-limited mechanisms rather than purely electrostatic interactions, due to topological constraints that resist rapid chain motion even as ionic screening rises.

Closer examination of the τ_D data on Fig. 7a suggests the presence of two distinct salt-dependent regimes. At low salt,

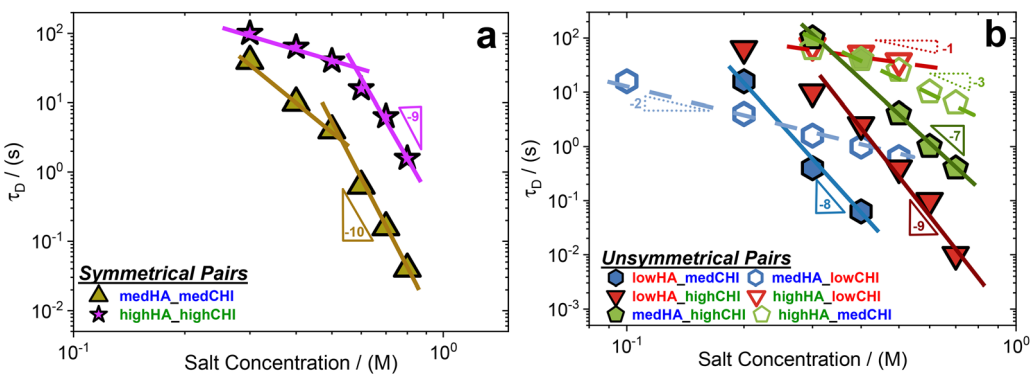

Fig. 7 Terminal relaxation dependence. Terminal relaxation time, τ_D, calculated as inverse of crossover frequency from the SAOS measurements studied as a function of the salt concentration for the symmetrical pairs (see legend) (a) and unsymmetrical pairs (see legend) (b). The lines in (a) and (b) are drawn as guides to the eyes. The respective scaling of the coacervate systems is reported with their corresponding colors in both panels. In panel (b), the dashed lines represent coacervate systems where the molecular weight of hyaluronic acid (M_{HA}), is smaller than the molecular weight of chitosan (M_{CHI}). And the solid line represents coacervate systems where $M_{HA} > M_{CHI}$.

relaxation slows as electrostatic crosslinks dominate the viscoelastic network, resulting in an extended transient gel-like structure. However, analysis of $\tan\delta$ as a function of salt concentration (Fig. S8) shows that no distinct crossover behavior is observed, unlike the case reported by Liu *et al.*,[30] where replotting frequency sweep data revealed a clear critical gel point. This indicates that our systems remain viscoelastic liquids across all salt concentrations and do not undergo a transition to a frequency-independent gel state. Beyond a critical salt concentration, screening of these interactions leads to the progressive breakdown of the percolated electrostatic network. Thus, the observed "network collapse" should not be interpreted as a critical gel point, but rather as a continuous transition from a strongly percolated to a transient, fluid-like network with shorter-lived associations. This interpretation is consistent with the framework proposed by Rubinstein *et al.*,[52] in which increasing ionic strength shifts the relaxation mechanism from electrostatically controlled to entanglement-limited dynamics.

This shift also implies a partial decoupling between electrostatic screening and network relaxation processes. As ionic strength increases, electrostatic correlations are rapidly screened, weakening ion-pair-mediated associations; however, relaxation of the entangled biopolymer network lags behind, being constrained by topological entanglements, chain stiffness, and hydration-mediated interactions. This temporal mismatch results in the breakdown of simple time–salt superposability, particularly in entangled HA–CHI systems.

The contrasting salt dependence of relaxation time between these symmetric systems highlights underlying differences in network resilience and chain relaxation modes. For medHA_medCHI, the medium molecular weight polymers form a moderately entangled network that is more readily disrupted by salt, resulting in a rapid drop in τ_D at relatively low concentrations. Beyond a certain salt content, where electrostatic interactions are already significantly screened and the network structure has largely collapsed, the relaxation time continues to decline steeply, with a scaling exponent of ~ -10 (see Fig. 7a), reflecting the transition to a more fluid-like, weakly connected state. This trend aligns with the findings from Rubinstein and coworker,[53] who demonstrated that salt progressively accelerates terminal relaxation by disrupting electrostatic bridges that mediate slow, cooperative chain dynamics.

In contrast, highHA_highCHI initially maintains a dynamically arrested state with slow relaxation due to its highly entangled structure. Yet, once the salt concentration surpasses a critical threshold, even this robust network experiences a collapse, marked by a sharper drop in τ_D (scaling of ~ -9, see Fig. 7a). Such behavior is in agreement with earlier work,[52] which observed that relaxation in symmetric coacervates softens at high salt only after the effective associative crosslinks break down, though entanglement offers transient mechanical resilience. These findings are consistent with prior literature, where both the persistence of electrostatic associations and the concentration of polymers within the coacervate phase are key determinants of salt-dependent dynamics.[2,41,59] In Fig. 7b, asymmetric systems are grouped by relative molecular weights of the polyanion (HA) and polycation (CHI). The systems where HA has a lower molecular weight than CHI (solid symbols: lowHA_medCHI, lowHA_highCHI, medHA_highCHI) show a strong dependence of τ_D on salt, with systems exhibiting scaling exponents of ~ -8, -9, -7, respectively (see Fig. 7b). This indicates that in these systems, dynamics are more electrostatically controlled; as salt increases, the screening of charge interactions rapidly enhances chain mobility and relaxation. These systems are more responsive to changes in ionic strength, and thus τ_D decreases more steeply. It is also noteworthy that the lowHA_highCHI system appears to exhibit two distinct scaling regimes, with a weaker dependence of τ_D on salt at low ionic strength and a steeper decrease at higher salt concentrations. This crossover likely reflects an initial regime where electrostatic associations dominate relaxation, followed by a transition at higher salt where screening disrupts these associations and dynamics become governed by polymer entanglement and residual physical interactions.

Conversely, in systems where HA has a higher molecular weight than CHI (open symbols: medHA_lowCHI, highHA_lowCHI, highHA_medCHI), the dependence of τ_D on salt is much weaker, with coacervates exhibiting power laws of ~ -2, -1, -3, respectively (see Fig. 7b). It is known that the HA is a stiffer polyanion (persistence length $\sim$4–10 nm) compared to the more flexible CHI (persistence length $\sim$1–4 nm at 90% DDA and pH 4.5).[66,67] These values correspond to the electrostatic component of chain stiffness, arising from intrachain charge repulsion and strongly dependent on ionic strength. Theoretical and simulation studies predict that the electrostatic persistence length decreases with increasing salt concentration, scaling approximately as $l_{p,e} \propto \kappa^{-n}$ $(1 \leq n \leq 2)$, where κ^{-1} is the Debye screening length.[81] Thus, as ionic strength increases, charge screening lowers the effective chain stiffness, particularly for flexible polyelectrolytes such as CHI. Under the salt conditions examined here (0–0.8 M NaCl), HA therefore remains relatively rigid due to its intrinsic backbone stiffness rather than its charge density, whereas CHI, with its higher linear charge density and more flexible backbone, undergoes a more pronounced reduction in electrostatic persistence length and correspondingly greater conformational adaptability. This stiffness reduces the capacity of HA to rapidly disentangle, rendering its relaxation modes slower and less responsive to ionic screening. Additionally, HA is highly hydrated, with structured water shells around its chains.[50,51,66] These hydration layers can act as physical barriers to rearrangement, slowing dynamics further. In contrast, long CHI chains, though entangled, remain more flexible and mobile, enabling faster relaxation when they dominate the entanglement network (as in the systems with low-M_w HA). These asymmetric trends reflect previous findings of Rubinstein *et al.*,[52] who noted that chain rigidity and low linear charge density (as in HA) lead to poor responsiveness to ionic screening, especially when the stiffer component dominates the network.

These results suggest that the dynamics of complex coacervates are more strongly governed by the molecular weight and the persistence length of the polyelectrolyte. When HA has a

high molecular weight, its inherent chain stiffness, slower disentanglement dynamics, and high hydration dominate the relaxation behavior, resulting in nearly salt-insensitive dynamics. In contrast, increasing the molecular weight of the more flexible CHI contributes to entanglement and elasticity, but the dynamics remain more responsive to salt, reflecting CHI's greater conformational adaptability. Thus, while both components contribute to coacervate rheology, it is the molecular weight and rigidity of the polyelectrolyte that primarily dictate the salt dependence of relaxation time in these systems. This interpretation aligns with the chain dynamics model of Aponte-Rivera *et al.*,[53] where polycation flexibility enables faster disentanglement and stronger salt sensitivity, while stiffer polyanions dominate slow relaxation modes.

Overall, Fig. 7 reinforces the importance of stiffness, entanglement, and hydration in determining the dynamic response of coacervate systems to ionic strength. This also provides a framework for tuning material properties in applications by selecting polymer pairs with strategic molecular weight and flexibility contrasts.

To further understand the salt-dependent mechanical behavior of the coacervates, the plateau modulus G_N^0 was extracted from the tan δ minimum of the frequency sweep measurements and plotted as a function of salt concentration for both symmetric and asymmetric systems in Fig. 8a and b, respectively.

In Fig. 8a, the symmetric coacervate systems, namely medHA_medCHI and highHA_highCHI, reveal two distinct regimes that reflect the changing physical state of the coacervate. In the range 0–0.5 M salt concentrations, the modulus of the two systems overlaps and decreases gradually. In this regime, the electrostatic interactions between oppositely charged chitosan and hyaluronic acid chains remain sufficiently strong to support a network. These interactions are partially screened by added salt, which reduces their effective range, but the polymer chains remain closely associated and the network retains much of its mechanical strength.[3,82,83] The coacervate phase at this stage is relatively dense, with limited water content, and the polymer chains are confined within a tight mesh that restricts their mobility. The modest decrease in modulus reflects small changes in the number and strength of these physical crosslinks. This behavior is consistent with the theoretical framework described by Rubinstein *et al.*,[52] who showed that in the low-salt regime, the dominant contribution to the modulus comes from the density of electrostatic crosslinks and the polymer concentration within the coacervate.

As the salt concentration increases beyond ~0.5 M, the modulus begins to decline more sharply. This transition marks a shift in the balance of forces governing coacervate structure. Electrostatic screening becomes strong enough to significantly weaken polymer–polymer attractions, reducing the number of associative contacts that form the elastic network. At the same time, the difference in chemical potential between the coacervate and the surrounding dilute phase becomes smaller, allowing more water to partition into the coacervate. This results in osmotic swelling and a lower polymer volume fraction.[5,8,84–88] The polymers become more solvated and gain conformational freedom, leading to increased chain mobility and a loss of network connectivity.[2,31,89,90] In this regime, the coacervate behaves more like a viscous fluid than a soft solid, and the drop in modulus reflects both dilution of the polymer phase and the loss of cohesive interactions.[5,28] Rubinstein *et al.*[52] further showed that this softening is governed by a salt-induced decrease in correlation length and reduction in electrostatic associations, both of which decrease the modulus nonlinearly. Moreover, Aponte-Rivera *et al.*[53] observed a similar two-regime behavior in symmetric complex coacervates, where the viscosity decreased weakly with salt at low concentrations, but showed a much steeper decay beyond a critical salt concentration. This behavior is attributed to the salt-induced changes in electrostatic interactions and correlation lengths.

Notably, highHA_highCHI displays a marginally weaker decrease compared to medHA_medCHI, with a scaling of ~−8 *vs.* ~−10, respectively (see Fig. 8a). This indicates that the higher molecular weight enhances entanglement density and physical crosslinking, thus modestly delaying the impact of ionic screening. Such a trend aligns with Rubinstein *et al.*[52]

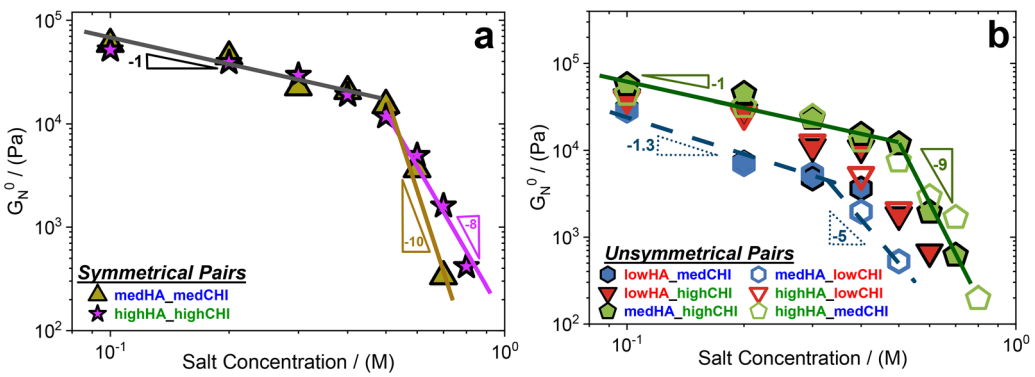

Fig. 8 Plateau modulus dependence. Plateau modulus G_N^0 as a function of the salt concentration for the symmetrical pairs (see legend) (a) and unsymmetrical pairs (see legend) (b). The lines in (a) and (b) are drawn as guides to the eyes. The respective scaling of the coacervate systems is reported with their corresponding colors in both panels. In panel (b), the dashed lines represent coacervate systems where the molecular weight of hyaluronic acid (M_{HA}) is greater than the molecular weight of chitosan (M_{CHI}). The solid line represents coacervate systems where $M_{HA} < M_{CHI}$.

scaling predictions, which indicate that higher chain lengths increase the number of entanglements per chain and reduce the modulus sensitivity to salt.

This phenomenon becomes more pronounced in asymmetric coacervate systems, where the direction of molecular weight mismatch between HA and CHI strongly influences the system's salt sensitivity. As observed in Fig. 8b, all asymmetric systems show a similar two-phase response: a faint plateau in modulus at low salt, followed by a steeper decline at higher salt concentrations. However, the sharpness of this decline varies systematically with the molecular weight asymmetry.

For systems where HA has a lower molecular weight than CHI, lowHA_medCHI, lowHA_highCHI, and medHA_highCHI (shown with solid symbols), the plateau modulus drops rapidly after the critical salt concentration. These systems incorporate long, flexible CHI chains and shorter, stiffer HA chains. Upon salt addition, the electrostatic crosslinks between HA and CHI are screened. However, the short HA chains lack sufficient flexibility to form alternative crosslinks or entanglements once electrostatic cohesion is weakened. As predicted by the correlation length framework, these smaller HA chains have a shorter correlation length, which becomes rapidly suppressed when the Debye length falls below their correlation length, upon addition of salt, leading to abrupt network disassembly and a sharp modulus drop.[53] As a result, the network collapses more abruptly, leading to a steep drop in modulus.

In contrast, systems where HA has a higher molecular weight than CHI: medHA_lowCHI, highHA_lowCHI, and highHA_medCHI (shown with open symbols), exhibit a more gradual decline in the plateau modulus. The long HA chains, though stiffer and less mobile, are more hydrated and structurally robust. Their extended contour length and persistent hydration shell support a more physically connected matrix even as salt concentration increases.[50,51] These chains are less responsive to ionic screening due to their lower effective linear charge density, arising from the extended chain conformation and extensive hydration shell, which reduce the local availability of charged groups for interpolymer association.[59] Additionally, these chains have a higher correlation length that remains above the Debye length over a wide range of salt concentrations.[53] Moreover, Aponte-Rivera *et al.*'s[53] theoretical framework implies that stiffer, longer polyelectrolytes might form more salt-resistant networks due to greater topological constraints and reduced chain mobility, which could slow the breakdown of the physical network. Consequently, these systems show a slower, more gradual decrease in modulus. Furthermore, the distinction between the above two categories of asymmetrical systems is quantified with the estimated slopes of the modulus decay: the medHA_highCHI system (solid green triangle) exhibits a steeper scaling of ~ -9, whereas medHA_lowCHI (dashed blue triangle) shows a more gradual scaling of ~ -5. This numerical difference supports the role of molecular weight asymmetry in governing the salt-induced softening behavior of asymmetric coacervates.

These results complement the behavior of symmetric systems (Fig. 8a) and highlight the additional complexity introduced by molecular weight asymmetry. In symmetric coacervates, the plateau modulus under ionic stress reflects chain entanglement balanced against electrostatic attraction, entropic ion release, and osmotic pressure driving water uptake. In asymmetric systems, however, modulus is further dictated by polyelectrolyte rigidity. When the longer chain is stiff, highly hydrated HA, the network remains salt-resilient; when the longer chain is flexible CHI, the network is more vulnerable to salt-induced disruption. These observations align with prior reports that increasing salt both accelerates relaxation and lowers polymer concentration in the coacervate phase, contributing to mechanical weakening at high ionic strength.[2,3,5,8,28,86,87] Taken together, the data underscore that both absolute M_w and the direction of asymmetry govern mechanical properties. This conclusion is consistent with relaxation time analysis (Fig. 7), where systems with long CHI chains exhibited faster dynamics and stronger salt sensitivity, while systems with long HA chains displayed slower relaxation and greater resilience.

Adhesion testing

Fig. 9 presents the adhesive behavior of various coacervate systems, highlighting how polymer asymmetry and molecular weight influence adhesion performance under varying salt concentrations. Panels 9a and b show representative stress–strain curves from probe tack experiments for the best and poorest performing coacervates, respectively, while panels 9c and d analyze the evolution of the work of adhesion (W_{adh}) as a function of salt concentration for symmetric and asymmetric systems. The full set of stress–strain curves used to determine W_{adh} values for panels 9c and d is included in the SI (Fig. S9).

In Fig. 9a, the three best-performing coacervates, 0 M lowHA_lowCHI, 0 M lowHA_medCHI, and 0 M highHA_highCHI, exhibit stress–strain curves characterized by broad stress plateaus and pronounced ''shoulders'' before failure. These shoulders in the stress–strain response typically signify cohesive deformation where the material continues to resist separation despite increasing strain.[5] This regime reflects a balance between elasticity (energy storage) and viscous flow (energy dissipation), enabling the coacervate to distribute and withstand mechanical stress over a larger strain range. Among these, 0 M lowHA_lowCHI shows the largest area under the curve, indicating the greatest energy dissipation and cohesive strength, followed by 0 M lowHA_medCHI and then 0 M highHA_highCHI. The superior performance of the lowHA_lowCHI system can be attributed to the presence of flexible, short chains that facilitate effective chain rearrangements and interfacial contact during deformation, enhancing adhesion. In contrast, the poorest-performing systems shown in Fig. 9b (0.4 M medHA_medCHI, 0.4 M medHA_highCHI, and 0.6 M medHA_highCHI) demonstrate a much steeper stress decay after reaching a lower peak stress, with minimal strain tolerance. These curves lack shoulders and plateau regions, reflecting a more brittle mechanical response with poor energy dissipation. The inability of these systems to maintain cohesive integrity under stress is linked to their reduced network connectivity at high salt

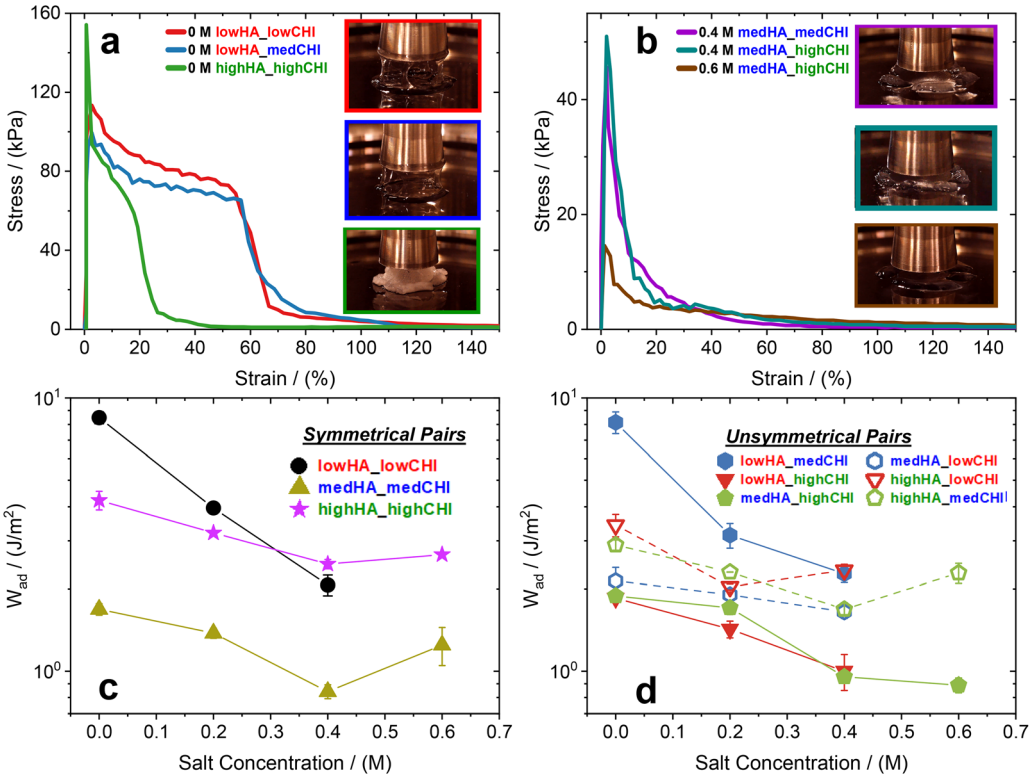

Fig. 9 Adhesion performance. Stress–strain curves of the probe tack experiments for (a) best performing coacervates (see legend, systems with the highest work of adhesion) and (b) poorest performing coacervates (see legend, systems with the lowest work of adhesion). The insets in (a) and (b) show the snapshots of the probe tack experiments for the best and poorest performing coacervates, respectively. The work of adhesion, estimated as the area under the curve of stress–strain curves, is studied as a function of the salt concentration for the symmetrical pairs (see legend) (c) and unsymmetrical pairs (see legend) (d). In panels (c) and (d), the solid and dashed lines are drawn as guides to the eye.

concentrations, where electrostatic interactions are heavily screened, and polymer dynamics become faster and less coordinated. In symmetric systems (Fig. 9c), the lowHA_lowCHI coacervate displays a high W_{adh} at low salt concentrations, with a sharp decrease as salt concentration increases. This behavior stems from the relatively unentangled nature of this system, where adhesion is predominantly governed by electrostatic interactions that are weakened upon salt addition. In contrast, the medHA_medCHI and highHA_highCHI systems exhibit significantly lower W_{adh} values and much weaker salt dependence. In this case, increased chain entanglement and higher polymer stiffness reduce sensitivity to ionic screening but also limit interfacial chain rearrangements, leading to lower adhesive energy overall. Interestingly, although highHA_highCHI forms a viscoelastic solid at 0 M, it performs poorly as an adhesive (compared to the lowHA_lowCHI and medHA_medCHI) due to the inherently slow relaxation dynamics of HA, its high hydration shell, and limited ability to make and break interfacial contacts quickly under dynamic stress.[50,51,66] The W_{adh} values observed here vary between 1–10 J m^{-2}. Similar work of adhesion has been reported for other coacervate systems (at the same retraction speed of 100 μm s^{-1}) in the literature.[5,6,13,91–95] Quite recently, P. Galland *et al.*[62] assessed the underwater adhesive and biological properties of HA/CHI coacervates. Though the authors do not explicitly report W_{adh} values, they do report the peak of stress–strain plots from their probe tack tests. In our work, we observe across the library of nine systems peak values ranging from ~20 kPa–~160 kPa (Fig. S9), which is in agreement with the values 10–70 kPa reported in the work of P. Galland *et al.*[62] The role of polymer asymmetry in tuning adhesion is highlighted in Fig. 9d. Here, the systems are divided into two groups based on the relative molecular weights of HA and CHI. Coacervates where HA has a lower molecular weight than CHI (lowHA_medCHI, lowHA_highCHI, and medHA_highCHI; shown with solid symbols) demonstrate a pronounced salt dependence in W_{adh}. These systems perform well under low-salt conditions, where electrostatic interactions dominate, but undergo significant loss of adhesion as salt concentration increases and screening reduces network cohesion. The high molecular weight CHI chains play a dominant role in network formation, and the relatively short HA chains are unable to maintain cohesion once ionic interactions are weakened. Conversely, systems where HA has a higher molecular weight than CHI (medHA_lowCHI, highHA_lowCHI, highHA_medCHI; shown with open symbols) show relatively weaker W_{adh} profiles across increasing salt concentrations. Such a weak salt dependence is a direct consequence of HA's intrinsic characteristics: its high stiffness (with a persistence length of 4–10 nm), low flexibility, and strong hydration shell create a coacervate matrix where relaxation and chain reorganization are inherently slow and less affected by ionic strength.[50,51,66] These systems likely form

entangled or semi-rigid networks in which the mechanical response is dominated by the more slowly relaxing HA component. These findings reveal a nuanced interplay between polymer molecular weight, asymmetry, flexibility, and ionic strength in dictating adhesive performance. In general, coacervates comprising flexible, low molecular weight chains exhibit high adhesion at low salt due to dynamic interfacial interactions but suffer a sharp performance drop at elevated salt levels. Systems with stiffer or higher molecular weight components, particularly those dominated by HA, display weaker but more salt-resilient adhesion. Thus, adhesive performance is not simply controlled by molecular weight or stiffness alone, but by the balance between chain flexibility, network connectivity, and dynamic responsiveness, all of which are tuned by the asymmetry in polyelectrolyte properties.

It is important to note that all probe tack experiments in this study were performed at a fixed retraction speed of 100 μm s^{-1} (see Experimental section) to maintain consistency. However, it is important to note that adhesive performance is highly dependent on the rate of debonding; different pulling speeds can alter the balance between cohesive dissipation and adhesive failure. While such rate-dependent studies are beyond the scope of the current work, they are essential for developing a more comprehensive understanding of coacervate adhesion mechanics.

Conclusions

This study demonstrates that molecular weight symmetry and asymmetry critically govern the rheological behavior, relaxation dynamics, and salt sensitivity of HA–CHI coacervates. Nearly all systems exhibit solid-like elasticity at zero salt, but increasing ionic strength accelerates relaxation dynamics and reduces the plateau modulus. Across all systems, the modulus follows a two-regime trend: a gradual decrease at low salt followed by a sharp decrease beyond a critical concentration. The sharpness of this transition is dictated by molecular weight asymmetry and chain rigidity: long, flexible CHI promotes strong adhesion at low salt but rapid loss of cohesion under ionic stress, whereas long, stiff HA confers slower, salt-resistant relaxation dynamics and a more gradual modulus decay. Time–salt superposition applies only to the unentangled system, while entangled systems exhibit multiple salt-dependent relaxation modes that preclude universal scaling.

These findings establish molecular-level design rules, showing that polymer stiffness and molecular weight are as important as charge density in determining coacervate resilience. The structure–property relationships identified here provide a framework for designing bio-derived adhesives and responsive soft materials. Future work will extend this approach to address charge asymmetry, an equally important factor in engineering coacervate mechanics.

Conflicts of interest

The authors declare no conflict of interest.

Data availability

Supplementary information (SI): linear viscoelasticity (additional frequency sweeps); adhesion testing (stress–strain curves from probe tack testing measurements). See DOI: **https://doi.org/10.1039/d5sm00910c**.

All raw and processed datasets underlying this study are available from the corresponding author upon reasonable request. This includes rheology frequency sweeps (G', G'', η^*), $\tan\delta$, and van Gurp–Palmen (vGP) outputs and shift factors, UV-vis transmittance data, and probe-tack stress–strain curves with adhesion work integrals, together with the associated metadata. Deposition of the complete raw datasets in a public repository is not feasible at this time because: (i) the primary data consist of instrument-native binary files generated by the Anton Paar MCR302e rheometer and the Hitachi U-1800 spectrophotometer, which require vendor software for full interpretation; and (ii) the total file volume is large (multi-gigabyte) across nine compositions, multiple salt concentrations, and independent replicates, making immediate public curation impractical without loss of fidelity. Upon request, we will provide the raw files, exported CSV summaries, and the analysis scripts used to compute $\tan\delta$, vGP plots, and time–salt shift factors, *via* a secure link or institutional repository.

References

1 E. Spruijt, J. Sprakel, M. Lemmers, M. A. C. Stuart and J. van der Gucht, *Phys. Rev. Lett.*, 2010, **105**, 208301.
2 E. Spruijt, M. A. Cohen Stuart and J. van der Gucht, *Macromolecules*, 2013, **46**, 1633–1641.
3 R. G. Larson, Y. Liu and H. Li, *J. Rheol.*, 2021, **65**, 77–102.
4 M. Khoonkari, J. Es Sayed, M. Oggioni, A. Amirsadeghi, P. Dijkstra, D. Parisi, F. Kruyt, P. van Rijn, M. K. Włodarczyk-Biegun and M. Kamperman, *Adv. Mater.*, 2023, **35**, 2210769.
5 L. van Westerveld, J. Es Sayed, M. de Graaf, A. H. Hofman, M. Kamperman and D. Parisi, *Soft Matter*, 2023, **19**, 8832–8848.
6 L. van Westerveld, T. Pelras, A. H. Hofman, K. Loos, M. Kamperman and J. Es Sayed, *Macromolecules*, 2024, **57**, 652–663.
7 Y. Liu, H. H. Winter and S. L. Perry, *Adv. Colloid Interface Sci.*, 2017, **239**, 46–60.
8 C. E. Sing and S. L. Perry, *Soft Matter*, 2020, **16**, 2885–2914.
9 A. H. Hofman, I. A. van Hees, J. Yang and M. Kamperman, *Adv. Mater.*, 2018, **30**, 1704640.
10 M. Dompé, F. J. Cedano-Serrano, O. Heckert, N. van den Heuvel, J. van der Gucht, Y. Tran, D. Hourdet, C. Creton and M. Kamperman, *Adv. Mater.*, 2019, **31**, 1808179.
11 A. D. Filippov, J. Sprakel and M. Kamperman, *Soft Matter*, 2021, **17**, 3294–3305.
12 J. Es Sayed, H. Brummer, M. C. A. Stuart, N. Sanson, P. Perrin and M. Kamperman, *ACS Macro Lett.*, 2022, **11**, 20–25.
13 M. Dompé, F. J. Cedano-Serrano, M. Vahdati, L. van Westerveld, D. Hourdet, C. Creton, J. van der Gucht, T. Kodger and M. Kamperman, *Adv. Mater. Interfaces*, 2020, **7**, 1901785.

14 I. A. van Hees, A. H. Hofman, M. Dompé, J. van der Gucht and M. Kamperman, *Eur. Polym. J.*, 2020, **141**, 110034.
15 M. Vahdati, D. Hourdet and C. Creton, *Prog. Polym. Sci.*, 2023, **139**, 101649.
16 N. Mendoza-Muñoz, G. Leyva-Gómez, E. Piñón-Segundo, M. L. Zambrano-Zaragoza, D. Quintanar-Guerrero, M. L. Del Prado Audelo and Z. Urbán-Morlán, *Int. J. Cosmet. Sci.*, 2023, **45**, 699–724.
17 A. Nolles, A. H. Westphal, J. A. de Hoop, R. G. Fokkink, J. M. Kleijn, W. J. H. van Berkel and J. W. Borst, *Biomacromolecules*, 2015, **16**, 1542–1549.
18 C. Schmitt and S. L. Turgeon, *Adv. Colloid Interface Sci.*, 2011, **167**, 63–70.
19 A. N. Kwant, J. S. Es Sayed, M. Kamperman, J. K. Burgess, D.-J. Slebos and S. D. Pouwels, *Adv. Healthcare Mater.*, 2025, **14**, 2402340.
20 A. N. Kwant, J. S. Es Sayed, N. Aledlbi, H. Pryshchepa, P. J. van der Zaag, J. K. Burgess, D.-J. Slebos, S. D. Pouwels and M. Kamperman, *Biomacromolecules*, 2025, **26**, 2433–2443.
21 E. N. Durmaz, M. I. Baig, J. D. Willott and W. M. de Vos, *ACS Appl. Polym. Mater.*, 2020, **2**, 2612–2621.
22 J. Es Sayed, A. Mukherjee, S. El Aani, N. Vengallur, M. Koch, A. Giuntoli and M. Kamperman, *Macromolecules*, 2024, **57**, 3190–3201.
23 A. Amirsadeghi, S. Mahdavi, P. Jager, M. Kamperman and J. Es Sayed, *Biomacromolecules*, 2025, **26**(6), 3641–3650.
24 X. Meng, Y. Du, Y. Liu, E. B. Coughlin, S. L. Perry and J. D. Schiffman, *Macromolecules*, 2021, **54**, 5033–5042.
25 J. Sun, S. L. Perry and J. D. Schiffman, *Biomacromolecules*, 2019, **20**, 4191–4198.
26 L. Zhou, H. Shi, Z. Li and C. He, *Macromol. Rapid Commun.*, 2020, **41**, 2000149.
27 F. Zhu, L. Cheng, J. Yin, Z. L. Wu, J. Qian, J. Fu and Q. Zheng, *ACS Appl. Mater. Interfaces*, 2016, **8**, 31304–31310.
28 J. Es Sayed, C. Caïto, A. Arunachalam, A. Amirsadeghi, L. van Westerveld, D. Maret, R. A. Mohamed Yunus, E. Calicchia, O. Dittberner, G. Portale, D. Parisi and M. Kamperman, *Macromolecules*, 2023, **56**, 5891–5904.
29 V. M. S. Syed and S. Srivastava, *ACS Macro Lett.*, 2020, **9**, 1067–1073.
30 Y. Liu, B. Momani, H. H. Winter and S. L. Perry, *Soft Matter*, 2017, **13**, 7332–7340.
31 F. J. Morin, M. L. Puppo and J. E. Laaser, *Soft Matter*, 2021, **17**, 1223–1231.
32 I. A. Ramírez Marrero, L. Boudreau, W. Hu, R. Gutzler, N. Kaiser, B. von Vacano, R. Konradi and S. L. Perry, *Macromolecules*, 2024, **57**, 4680–4694.
33 M. Yang, J. Shi and J. B. Schlenoff, *Macromolecules*, 2019, **52**, 1930–1941.
34 Y. Liu, C. F. Santa Chalarca, R. N. Carmean, R. A. Olson, J. Madinya, B. S. Sumerlin, C. E. Sing, T. Emrick and S. L. Perry, *Macromolecules*, 2020, **53**, 7851–7864.
35 J. Sun, J. D. Schiffman and S. L. Perry, *ACS Appl. Polym. Mater.*, 2022, **4**, 1617–1625.
36 Y. Jin, S. Lu, X. Chen, Q. Fang, X. Guan, L. Qin, C. Chen and C. Zhao, *Macromolecules*, 2024, **57**, 2746–2755.
37 A. B. Marciel, S. Srivastava and M. V. Tirrell, *Soft Matter*, 2018, **14**, 2454–2464.
38 F. G. Hamad, Q. Chen and R. H. Colby, *Macromolecules*, 2018, **51**, 5547–5555.
39 S. Ali and V. M. Prabhu, *Gels*, 2018, **4**(1), 11.
40 R. F. Shamoun, H. H. Hariri, R. A. Ghostine and J. B. Schlenoff, *Macromolecules*, 2012, **45**, 9759–9767.
41 K. Akkaoui, M. Yang, Z. A. Digby and J. B. Schlenoff, *Macromolecules*, 2020, **53**, 4234–4246.
42 S. M. Lalwani, P. Batys, M. Sammalkorpi and J. L. Lutkenhaus, *Macromolecules*, 2021, **54**, 7765–7776.
43 P. C. Suarez-Martinez, P. Batys, M. Sammalkorpi and J. L. Lutkenhaus, *Macromolecules*, 2019, **52**, 3066–3074.
44 M. Tekaat, D. Bütergerds, M. Schönhoff, A. Fery and C. Cramer, *Phys. Chem. Chem. Phys.*, 2015, **17**, 22552–22556.
45 K. Sadman, Q. Wang, Y. Chen, B. Keshavarz, Z. Jiang and K. R. Shull, *Macromolecules*, 2017, **50**, 9417–9426.
46 M. Van Gurp and J. Palmen, *Rheol. Bull.*, 1998, **67**, 5–8.
47 R. Salehiyan, S. S. Ray, F. J. Stadler and V. Ojijo, *Materials*, 2018, **11**(12), 2450.
48 U. G. Centa, A. Oseli, M. Mihelčič, A. Kralj, M. Žnidaršič, M. Halilovič and L. S. Perše, *Polymers*, 2024, **16**(1), 22.
49 R. A. Mohamed Yunus and D. Parisi, *Biomacromolecules*, 2024, **25**, 6883–6898.
50 M. Bathe, G. C. Rutledge, A. J. Grodzinsky and B. Tidor, *Biophys. J.*, 2005, **88**, 3870–3887.
51 G. Giubertoni, A. Pérez de Alba Ortíz, F. Bano, X. Zhang, R. J. Linhardt, D. E. Green, P. L. DeAngelis, G. H. Koenderink, R. P. Richter, B. Ensing and H. J. Bakker, *Macromolecules*, 2021, **54**, 1137–1146.
52 M. Rubinstein, Q. Liao and S. Panyukov, *Macromolecules*, 2018, **51**, 9572–9588.
53 C. Aponte-Rivera and M. Rubinstein, *Macromolecules*, 2021, **54**, 1783–1800.
54 R. Shi, T. L. Sun, F. Luo, T. Nakajima, T. Kurokawa, Y. Z. Bin, M. Rubinstein and J. P. Gong, *Macromolecules*, 2018, **51**, 8887–8898.
55 G. Lalevée, L. David, A. Montembault, K. Blanchard, J. Meadows, S. Malaise, A. Crépet, I. Grillo, I. Morfin, T. Delair and G. Sudre, *Soft Matter*, 2017, **13**, 6594–6605.
56 G. Lalevée, G. Sudre, A. Montembault, J. Meadows, S. Malaise, A. Crépet, L. David and T. Delair, *Carbohydr. Polym.*, 2016, **154**, 86–95.
57 O. Karabiyik Acar, A. B. Kayitmazer and G. Torun Kose, *Biomacromolecules*, 2018, **19**, 1198–1211.
58 A. B. Kayitmazer, A. F. Koksal and E. Kilic Iyilik, *Soft Matter*, 2015, **11**, 8605–8612.
59 A. B. Kayitmazer, F. Comert, H. H. Winter and P. B. Messersmith, *Biomolecules*, 2022, **12**(12), 1817.
60 S. L. Perry, Y. Li, D. Priftis, L. Leon and M. Tirrell, *Polymers*, 2014, **6**, 1756–1772.
61 D. Priftis and M. Tirrell, *Soft Matter*, 2012, **8**, 9396–9405.
62 P. Galland, M. H. Iqbal, D. Favier, M. Legros, P. Schaaf, F. Boulmedais and M. Vahdati, *J. Colloid Interface Sci.*, 2024, **661**, 196–206.

63 P. M. Biesheuvel and M. A. Cohen Stuart, *Langmuir*, 2004, **20**, 2785–2791.
64 F. Akcay Ogur, S. Mamasoglu, S. L. Perry, F. A. Akin and A. B. Kayitmazer, *J. Phys. Chem. B*, 2024, **128**, 9022–9035.
65 R. Chollakup, J. B. Beck, K. Dirnberger, M. Tirrell and C. D. Eisenbach, *Macromolecules*, 2013, **46**, 2376–2390.
66 E. Buhler and F. Boué, *Macromolecules*, 2004, **37**, 1600–1610.
67 S. Morariu, C.-E. Brunchi and M. Bercea, *Ind. Eng. Chem. Res.*, 2012, **51**, 12959–12966.
68 E. D. Atkins, C. F. Phelps and J. K. Sheehan, *Biochem. J.*, 1972, **128**, 1255–1263.
69 S. Trzciński, K. M. Vårum, D. U. Staszewska, O. Smidsrød and M. Bohdanecký, *Carbohydr. Polym.*, 2002, **48**, 171–178.
70 M. Rubinstein and R. H. Colby, *Polymer physics*, Oxford University Press, 2003.
71 K. Kremer and G. S. Grest, *J. Chem. Phys.*, 1990, **92**, 5057–5086.
72 M. Doi, S. F. Edwards and S. F. Edwards, *The theory of polymer dynamics*, Oxford University Press, 1988, vol. 73.
73 R. A. Mohamed Yunus, M. Koch, P. Dieudonné-George, D. Truzzolillo, R. H. Colby and D. Parisi, *ACS Macro Lett.*, 2024, **13**, 219–226.
74 D. Truzzolillo, D. Marzi, J. Marakis, B. Capone, M. Camargo, A. Munam, F. Moingeon, M. Gauthier, C. N. Likos and D. Vlassopoulos, *Phys. Rev. Lett.*, 2013, **111**, 208301.
75 D. Parisi, D. Truzzolillo, D. Vishnu D, M. Gauthier and D. Vlassopoulos, *Macromolecules*, 2019, **52**(15), 5872–5883.
76 D. Parisi, M. Camargo, K. Makri, M. Gauthier, C. N. Likos and D. Vlassopoulos, *J. Chem. Phys.*, 2021, **155**, 34901.
77 D. Truzzolillo, D. Vlassopoulos, A. Munam and M. Gauthier, *J. Rheol.*, 2014, **58**, 1441–1462.
78 D. Parisi, D. Truzzolillo, A. H. Slim, P. Dieudonné-George, S. Narayanan, J. C. Conrad, V. D. Deepak, M. Gauthier and D. Vlassopoulos, *Macromolecules*, 2023, **56**, 1818–1827.
79 S. Meng, J. M. Ting, H. Wu and M. V. Tirrell, *Macromolecules*, 2020, **53**, 7944–7953.
80 Y. Hong, S. Yoo, J. Han, J. Kim, Y. Lee, Y. Jho, Y. S. Kim and D. S. Hwang, *Commun. Chem.*, 2024, **7**, 182.
81 M. Ullner, B. Jönsson, C. Peterson, O. Sommelius and B. Söderberg, *J. Chem. Phys.*, 1997, **107**, 1279–1287.
82 Q. Wang and J. B. Schlenoff, *Macromolecules*, 2014, **47**, 3108–3116.
83 H. Li, Y. Liu, A. Shetty and R. G. Larson, *J. Rheol.*, 2022, **66**, 1067–1077.
84 S. S. Ribeiro, N. Samanta, S. Ebbinghaus and J. C. Marcos, *Nat. Rev. Chem.*, 2019, **3**, 552–561.
85 H. M. Fares, Q. Wang, M. Yang and J. B. Schlenoff, *Macromolecules*, 2019, **52**, 610–619.
86 L. Li, S. Srivastava, M. Andreev, A. B. Marciel, J. J. de Pablo and M. V. Tirrell, *Macromolecules*, 2018, **51**, 2988–2995.
87 F. van Riel Neto, C. Borbeck, T. H. Saatkamp, M. Kenny, S. Schmidt and P. Gilch, *Chem.:Methods*, 2025, 2500005.
88 D. Priftis, K. Megley, N. Laugel and M. Tirrell, *J. Colloid Interface Sci.*, 2013, **398**, 39–50.
89 S. Chen and Z.-G. Wang, *Proc. Natl. Acad. Sci. U. S. A.*, 2022, **119**, e2209975119.
90 T. Lu and E. Spruijt, *J. Am. Chem. Soc.*, 2020, **142**, 2905–2914.
91 M. Vahdati, F. J. Cedano-Serrano, C. Creton and D. Hourdet, *ACS Appl. Polym. Mater.*, 2020, **2**, 3397–3410.
92 M. Dompé, M. Vahdati, F. van Ligten, F. J. Cedano-Serrano, D. Hourdet, C. Creton, M. Zanetti, P. Bracco, J. van der Gucht, T. Kodger and M. Kamperman, *ACS Appl. Polym. Mater.*, 2020, **2**, 1722–1730.
93 M. Dompé, F. J. Cedano-Serrano, M. Vahdati, D. Hourdet, J. van der Gucht, M. Kamperman and T. E. Kodger, *Polymers*, 2020, **12**(2), 320.
94 M. Dompé, F. J. Cedano-Serrano, M. Vahdati, U. Sidoli, O. Heckert, A. Synytska, D. Hourdet, C. Creton, J. van der Gucht, T. Kodger and M. Kamperman, *Int. J. Mol. Sci.*, 2020, **21**(1), 100.
95 A. Arunachalam, T. Oosterhoff, I. Breet, P. Dijkstra, R. A. Mohamed Yunus, D. Parisi, B. Knegt, M. Macel and M. Kamperman, *Commun. Mater.*, 2025, **6**, 101.